2-1-2007

The Wind-ISM Interaction of α Tauri

Brian E. Wood
University of Colorado Boulder

Graham M. Harper
University of Colorado Boulder

Hans-Reinhard Muller
Dartmouth College

Jacob Heerikhuisen
University of California, Riverside

Gary P. Zank
University of California, Riverside

The Astrophysical Journal, 655:946–957, 2007 February 1

THE WIND-ISM INTERACTION OF α TAURI[1]

Brian E. Wood,[2] Graham M. Harper,[3] Hans-Reinhard Müller,[4,5] Jacob Heerikhuisen,[5] and Gary P. Zank[5]

Received 2006 July 20; accepted 2006 October 24

ABSTRACT

Ultraviolet spectra of α Tau (K5 III) obtained by the *Hubble Space Telescope* (*HST*) show many emission lines affected by broad absorption from the strong wind of this red giant star. For the Mg II *h* and *k* lines there is also a narrow absorption feature in the midst of the wind absorption that has been interpreted as being from α Tau's wind–interstellar medium (ISM) interaction region (i.e., its "astrosphere"). We try to reproduce this absorption using hydrodynamic models of the α Tau astrosphere, which show that stellar wind material heated, compressed, and decelerated at the wind's termination shock (TS) can produce significant absorption at about the right velocity. By experimenting with different model input parameters, we find that the parameter that the absorption is most sensitive to is the ISM pressure, which determines the location of and therefore the density at the TS. However, the models underestimate both the amount of deceleration at the TS and the amount of absorption for realistic input parameters. We demonstrate that these problems can in principle be resolved by modeling the TS as a radiative shock. However, a cooling timescale short enough to affect the postshock flow is only attainable if α Tau's wind speed is increased from the 27–30 km s^{-1} values derived from fits to wind absorption to at least 35 km s^{-1}. The models also seem to require a very high ISM pressure of $P/k \approx 30{,}000$ cm^{-3} K to induce densities at the TS high enough to yield sufficient radiative cooling. This pressure is at least a factor of 2 higher than other estimates of ISM thermal pressure within the Local Bubble.

Subject headings: circumstellar matter — stars: individual (α Tauri) — stars: winds, outflows — ultraviolet: stars

Online material: color figure

1. INTRODUCTION

Red giants with K spectral types are typically found to have warm stellar winds ($T \sim 10^4$ K) with modest mass-loss rates of $\dot{M} \sim 10^{-11}$ to $10^{-10}\,M_\odot$ yr^{-1}. The properties of these winds are most commonly determined by analyzing the broad absorption they produce in strong chromospheric resonance lines such as Mg II *h* and *k* at 2803.5 and 2796.4 Å, respectively. One of the closest and brightest red giants is the K5 III star α Tau (Aldebaran, HD 29139), at a distance of only $d = 20.0 \pm 0.4$ pc (Perryman et al. 1997).

In their extensive analysis of *Hubble Space Telescope* (*HST*) UV spectra of α Tau's chromospheric emission lines and their broad wind absorption features, Robinson et al. (1998) note the existence of a narrow Mg II absorption feature near the rest frame of the star. Figure 1 plots the Mg II *h* and *k* lines on a heliocentric velocity scale, showing the narrow absorption only slightly blueshifted from the stellar rest frame ($V_{\rm rad} = 54.3$ km s^{-1}). This absorption appears very much like an interstellar medium (ISM) absorption feature, but it is not in the right location. The local ISM flow vector of Lallement et al. (1995), which should be reasonably accurate for our purposes due to α Tau's close proximity, predicts an ISM velocity of 25.5 km s^{-1} for the α Tau line of sight. No absorption is seen at this velocity in Figure 1 simply because the stellar wind absorption is saturated at that location. This is true for most other lines as well, but Redfield & Linsky (2004a) find interstellar D I Lyα absorption at about the expected location. The narrow Mg II absorption feature is over 25 km s^{-1} away from this ISM absorption. Although multiple ISM velocity components are often seen even for very short lines of sight, they are not generally so widely separated as this. A survey of all *HST*-observed ISM Mg II absorption features within 100 pc by Redfield & Linsky (2002) makes it clear that finding an ISM absorption component so far from the velocity predicted by the local flow vector is extremely unlikely.

Because of its location close to the rest frame of the star, Robinson et al. (1998) proposed instead that the narrow absorption is from the interaction region between α Tau's wind and the ISM, i.e., its "astrosphere" (analogous to "heliosphere"). The absorption must certainly originate farther from the star than where α Tau's stellar wind is opaque to Mg II photons, or wind scattering would destroy the feature. If the absorption cannot be stellar or interstellar, an astrospheric origin is then practically the only interpretation left.

If the astrospheric interpretation is correct, the Mg II absorption feature is then somewhat analogous to the astrospheric H I Lyα absorption that has previously been detected for many cool main-sequence stars (Wood et al. 2005b). With the assistance of hydrodynamic models of the astrospheres, the Lyα absorption has proven to be very useful for estimating properties of solar-like stellar winds that are otherwise undetectable (Wood et al. 2005a). We here attempt to model α Tau's astrosphere in a similar manner. We hope to see whether these models can reproduce the Mg II absorption, and by experimenting with different ISM and stellar wind input parameters we then explore the diagnostic power of the absorption.

2. α TAU'S WIND PROPERTIES

Before modeling α Tau's astrosphere, we must first estimate the properties of its stellar wind. This is done by modeling the Mg II

[1] Based on observations with the NASA/ESA *Hubble Space Telescope*, obtained at the Space Telescope Science Institute, which is operated by the Association of Universities for Research in Astronomy, Inc., under NASA contract NAS5-26555.

[2] JILA, University of Colorado, Boulder, CO; woodb@origins.colorado.edu.

[3] Center for Astrophysics and Space Astronomy, Astrophysics Research Laboratory, University of Colorado, Boulder, CO; gmh@casa.colorado.edu.

[4] Department of Physics and Astronomy, Dartmouth College, Hanover, NH; hans.mueller@dartmouth.edu.

[5] Institute of Geophysics and Planetary Physics, University of California at Riverside, Riverside, CA; jacobh@ucr.edu, zank@ucr.edu.

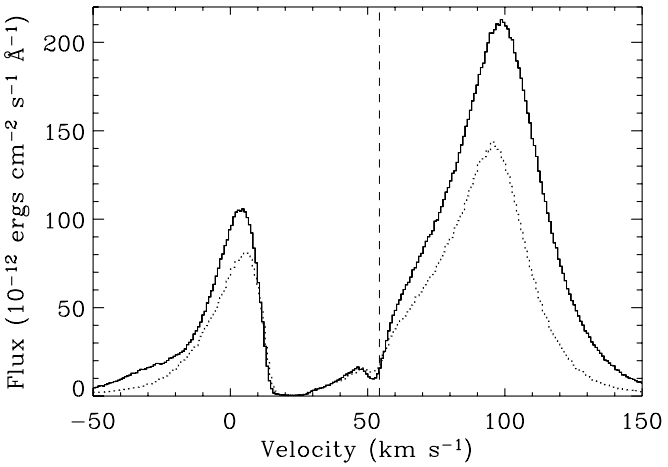

FIG. 1.—Mg II *h* and *k* lines of α Tau (*dotted and solid lines, respectively*), plotted on a heliocentric velocity scale. The dashed line indicates the stellar rest frame. The line profiles are dominated by very broad wind absorption, but there is also a narrow absorption feature near the stellar rest frame that is believed to be astrospheric in nature.

wind absorption features (see Fig. 1). The Mg II spectrum we analyze is the 1994 April 8 *HST* observation taken using the Goddard High Resolution Spectrograph (GHRS) instrument. The spectrum is an 862 s exposure through the small science aperture (SSA) with the Ech-B grating, which provides a superb spectral resolution of about 3 km s^{-1}. We processed the data using the IDL-based CALHRS calibration software (Robinson et al. 1992). There was a second GHRS Ech-B observation of α Tau's Mg II lines on 1996 October 15, but the wind absorption and the narrow astrospheric absorption feature in these data are essentially the same as in 1994.

The physical size of α Tau, important for quantitative studies of stellar winds, is well determined. The *Hipparcos* parallax is 50.09 ± 0.95 mas. Combined with a mean limb-darkened angular diameter of 20.58 ± 0.03 mas, based on interferometric techniques and lunar occultation measurements, this implies a radius of $R_* = 44.2 \pm 0.9\ R_\odot$ (Richichi & Roccatagliata 2005).

We refer the reader to Harper et al. (1995) for details on our Mg II wind absorption modeling procedure, which leads to a mass-loss rate estimate of $\dot{M} \simeq 1 \times 10^{-11}\ M_\odot\ \mathrm{yr}^{-1}$, a wind terminal velocity of $V_w = 27$ km s^{-1}, and a turbulence of $V_{\mathrm{turb}} = 14$ km s^{-1}, assuming a constant isotropic turbulence throughout the wind. This mass-loss rate assumes that magnesium is entirely singly ionized within the wind. The uncertainty in the analysis is dominated by systematic unknowns such as the gradient in the wind turbulence and the wind velocity law. These measurements are consistent with those of Robinson et al. (1998) using the Sobolev with Exact Integration (SEI) method for Fe II and O I wind scattered profiles, which are also sensitive to the same systematic uncertainties. They find $\dot{M} \simeq 1.6 \times 10^{-11}\ M_\odot\ \mathrm{yr}^{-1}$, $V_w = 30$ km s^{-1}, and $V_{\mathrm{turb}} = 24$ km s^{-1}. Both analyses suggest a quite rapid wind acceleration, with the wind reaching half the terminal velocity within three stellar radii above the photosphere. The H and K lines of Ca II, which is a minority species (Harper et al. 2004), show weak circumstellar absorption features that vary in velocity and depth on month timescales (Reimers 1977). These timescales are consistent with the spatial scales inferred for the wind acceleration region derived from the UV line profiles.

Continuum flux measurements at centimeter wavelengths provide upper limits to the characteristic electron temperature for different layers in the atmosphere. The radio opacity increases strongly with wavelength ($\propto \lambda^{2.1}$), so the longest wavelengths sample the outermost layers. The emission is thermal continuum, so the source function is the Planck function in the Rayleigh-Jeans tail, which is linear in electron temperature. Since the characteristic angular diameter of the radio-emitting region is larger than the known photospheric angular diameter, each centimeter-wavelength flux provides an upper limit to the characteristic electron temperature. On 1989 December 24, α Tau was observed at 2 and 3.6 cm with the NRAO Very large Array (VLA)[6] and was detected with fluxes (and 1 σ errors) of 0.86 ± 0.13 and 0.30 ± 0.04 mJy, respectively (S. Drake 2006, VLA program AD0238, private communication; Wendker 1995). On 1997 September 27, A. Brown and G. Harper (VLA program AB0845) obtained fluxes of 0.95 ± 0.08 and 0.28 ± 0.03 mJy at 2 and 3.6 cm, respectively, with a 3 σ upper limit of 0.07 mJy at 6 cm. These 1997 values correspond to electron temperatures of $<$17,700 and $<$16,200 K, respectively, and a 3 σ upper limit of $<$12,300 K. The effective electron temperature is therefore declining with radius, and the 6 cm flux upper limit provides a good estimate for the upper limit for the electron temperature at the base of the wind. The UV mass-loss rate estimates are consistent with these fluxes and a previous 6 cm upper limit (Drake & Linsky 1986).

Another temperature that can be estimated is the ionization temperature, which can be inferred from the ionization states of lines that are observed to show wind absorption. The UV spectra taken by *HST* provide the best selection of lines to look at for these purposes. The full GHRS data set has been discussed by Robinson et al. (1998), but in the far-UV the best data are from a 2002 January 3 observation by the Space Telescope Imaging Spectrograph (STIS) instrument, which replaced GHRS in 1997. STIS observed the 1150–1710 Å spectral region for 10.5 ks with the E140M grating, which has a spectral resolution of about 7 km s^{-1}. This spectrum was previously reduced and analyzed by Ayres et al. (2003). Lines in the *HST* spectra that show the broad wind absorption includes Mg II *h* and *k*, the O I triplet near 1300 Å, the C II $\lambda\lambda$1334, 1335 lines, Si II λ1526, and various Fe II lines in the near-UV. No wind absorption is seen for lines formed at hotter temperatures such as Si III λ1206, the Si IV $\lambda\lambda$1393, 1402 lines, and the C IV $\lambda\lambda$1548, 1550 doublet (Ayres et al. 2003). The relative opacities of the strong UV scattering lines are shown in Harper (2001) as a function of ionization temperature. Above 16,000 K, Mg II and O I rapidly ionize to the next stage, while Si II becomes Si III. The difference in wind scattering between Si III (none) and Mg II and Si II (strong) suggests an ionization temperature of $<$16,000 K. No absorption is apparent for the C I UV1 multiplet lines at 1656 Å, suggesting that C II must be the dominant ionization state of carbon in the wind.

The astrospheric models presented in § 4 require wind properties at 1 AU from the star as an inner boundary condition. These properties are listed in Table 1 for the various models that we compute. Most models assume our best-fit wind speed of $V_w = 27$ km s^{-1}, but we also experiment with a higher speed of $V_w = 35$ km s^{-1} in models 8–10. The mass-loss rate of α Tau is rather modest, shows no evidence for dust, and is probably driven by processes involving magnetic fields. The thermal energy balance is controlled by numerous cooling and heating processes. The cooling is from wind expansion and acceleration together with radiative cooling by atomic and singly ionized species. The heating is from the deposition of magnetic wave energy, ambipolar diffusion, and radiative heating (Harper 2001). The thermal temperature under these conditions can be nonmonotonic with radius,

[6] The National Radio Astronomy Observatory is a facility of the National Science Foundation operated under cooperative agreement by Associated Universities, Inc.

TABLE 1
Model Input Parameters

		Stellar Wind Parameters at 1 AU				ISM Parameters				
Model No.	Type of Model	n_w(H I) (cm^{-3})	$n_w(H^+)$ (cm^{-3})	V_w (km s^{-1})	T_w (K)	n_∞(H I) (cm^{-3})	$n_\infty(H^+)$ (cm^{-3})	V_∞ (km s^{-1})	T_∞ (K)	θ (deg)
1.....	Two-fluid	3×10^4	5×10^3	27	7500	0	4×10^{-3}	34	5×10^5	149
2.....	Two-fluid	3×10^4	5×10^3	27	7500	0	4×10^{-3}	44	5×10^5	170
3.....	Kinetic	3×10^4	5×10^3	27	7500	0	4×10^{-3}	44	5×10^5	170
4.....	Two-fluid	3×10^5	5×10^4	27	7500	0	4×10^{-3}	34	5×10^5	149
5.....	Two-fluid	3×10^4	5×10^3	27	7500	0	0.02	44	5×10^5	170
6.....	Two-fluid	3×10^4	5×10^3	27	7500	0	0.02	44	1.5×10^6	170
7.....	Two-fluid	3×10^4	5×10^2	27	7500	0	0.02	44	1.5×10^6	170
8.....	Two-fluid	3×10^4	3.3×10^3	35	7500	0	0.01	44	5×10^5	170
9.....	Two-fluid	3×10^4	3.3×10^3	35	7500	0	0.03	44	5×10^5	170
10.....	Two-fluid	3×10^4	5×10^3	35	7500	0	0.02	44	5×10^5	170

especially near the stellar surface. Based on the electron and ionization temperature constraints mentioned above, we estimate a crude wind temperature of 7500 K at 1 AU. The stellar mass-loss rate and wind velocity can be used to infer the wind density at 1 AU. At a temperature of ~7500 K, we expect hydrogen in the wind to be mostly neutral. Assuming hydrogen is predominantly neutral, we compute an H I density at 1 AU of $n_w(\mathrm{H\ I}) = 3.5 \times 10^4$ cm^{-3}. This is the density assumed in most of the models, but in model 4 we experiment with a much higher density. The exact ionization state of H is rather uncertain, but Harper et al. (2004) find a lower limit of $x_e > 0.01$ for the hydrogen ionization by requiring that Ca III recombine to Ca II in the accelerating outflow, in order to explain the existence of Ca II wind absorption. Here we experiment with ionization fractions in the range $x_e = 0.016$–0.16 (see Table 1). With the advection properties of α Tau's wind flow, the ionization fraction quickly "freezes in" to a near-constant value.

3. INTERSTELLAR BOUNDARY CONDITIONS

Besides the stellar wind properties, we also need to estimate the properties of the ambient interstellar medium before we can model α Tau's astrosphere. Both α Tau and the Sun lie within the Local Bubble (LB), a region of generally low ISM densities extending roughly 100 pc from the Sun in most directions (Sfeir et al. 1999; Lallement et al. 2003). Most of the volume of the bubble is believed to be very hot, ionized plasma, which produces much of the soft X-ray background emission (Snowden et al. 1998).

There are various small, warm, partially neutral clouds embedded within the LB. It just so happens that the Sun lies within one of these, the local interstellar cloud (LIC). Redfield & Linsky (2000) estimate a diameter of 5–7 pc for the LIC. At a distance of 20.0 pc α Tau lies well beyond the edge of the LIC, suggesting that α Tau will likely be within the hot ISM that dominates the LB. Further evidence for this is provided by the measured deuterium column density for this line of sight, $\log N(\mathrm{D\ I}) = 12.99$ (Redfield & Linsky 2004a). Assuming that $\mathrm{D/H} = 1.56 \times 10^{-5}$, a ratio that has been shown to apply throughout the LB (Wood et al. 2004), we infer a very low ISM H I column density of $\log N(\mathrm{H\ I}) = 17.80$. This is even lower than the $\log N(\mathrm{H\ I}) = 18.15$ column density that Redfield & Linsky (2000) predict for the amount of LIC material for this line of sight.

There is therefore no evidence for any neutral material along this line of sight beyond that of the LIC, so the implication is once again that it is very likely that α Tau is surrounded by the hot, ionized ISM within the LB rather than the cooler, partially neutral material that surrounds the Sun. The hot LB plasma accounts for much of the soft X-ray background, and *ROSAT* (*Röntgensatellit*) observations of this emission suggest a temperature of $T = 10^{6.07 \pm 0.05}$ K and a pressure of $P/k \approx 15{,}000$ cm^{-3} K, assuming that the LB is in collisional ionization equilibrium and has solar abundances (Snowden et al. 1998).

However, the *ROSAT* measurements are controversial. The thermal pressures of warm clouds in the LB, such as the LIC, are only $P/k \approx 2280$ cm^{-3} K (Jenkins 2002; Redfield & Linsky 2004b). Such a large pressure imbalance between the LB hot plasma and the cooler clouds scattered within it seems unlikely. In principle, the imbalance could be rectified by proposing substantial magnetic pressure within the LIC and other such clouds. However, this would require high field strengths of at least $B = 7$ μG, and for fields greater than $B = 3$–4 μG heliospheric models generally predict a termination shock closer to the Sun than the distance of 94 AU found by *Voyager 1* (Gloeckler et al. 1997; Stone et al. 2005). This problem can be mitigated by proposing that the LIC field is oriented close to parallel with the ISM flow seen by the heliosphere, but this assumption may be inconsistent with the observed deflection of interstellar H atoms in the heliosphere, which is believed to be due to an ISM field skewed with respect to the ISM flow (Florinski et al. 2004; Izmodenov et al. 2005; Lallement et al. 2005).

There are other suggestions that the LB pressure estimated from the *ROSAT* data is too large. Some of the X-ray background that had been assumed to be entirely from the hot LB material may instead have a different origin. Some of the soft X-ray background is now believed to be from charge exchange between the solar wind and inflowing interstellar neutrals within our own heliosphere (Cravens 2000; Lallement 2004a). It has also been proposed that some of the soft X-ray background could be from charge exchange induced emission from the boundary of the LB (Lallement 2004b). Finally, observations from the *Cosmic Hot Interstellar Plasma Spectrometer* (*CHIPS*) satellite seem to suggest much lower X-ray emissivity than the *ROSAT* observations (Hurwitz et al. 2005). These discrepancies might be resolved by assuming a somewhat lower temperature ($T \approx 10^{5.8}$ K) and heavy metal depletion within the LB (Bellm & Vaillancourt 2005). Breitschwerdt (2001) has proposed abandoning collisional ionization equilibrium entirely in modeling the LB X-ray emission, which would allow LB temperatures to be much lower than generally assumed ($T \sim 10^5$ K), and with lower pressures in better agreement with those of the warm clouds embedded within the LB.

Our astrospheric models experiment with a wide range of assumed ISM pressures (see Table 1). For example, the temperature and proton density assumed for model 1, $T_\infty = 5 \times 10^5$ K

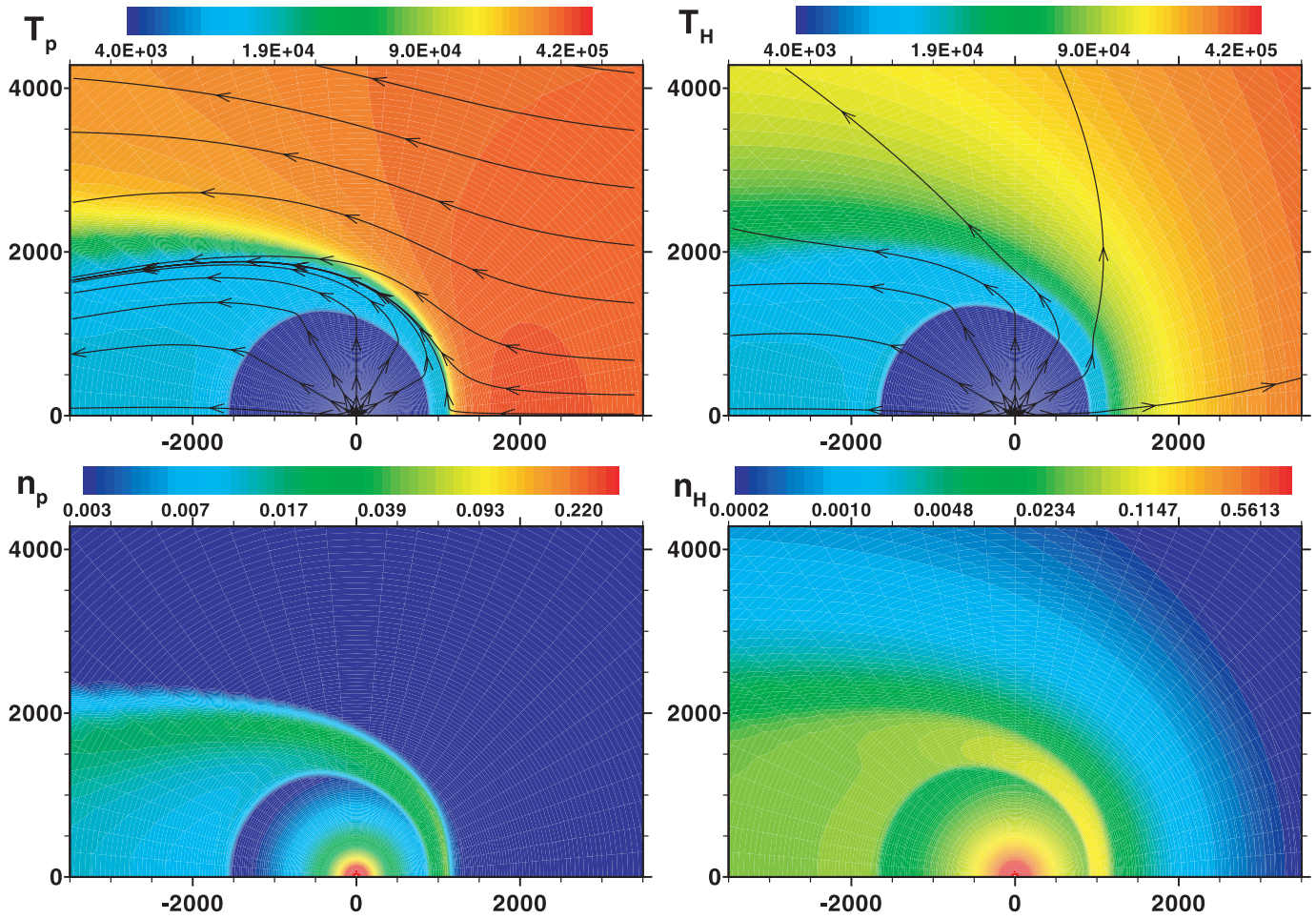

FIG. 2.—Hydrodynamic model of the α Tau astrosphere for model 1, where the top panels are the proton and H I temperatures and the bottom panels are the proton and H I densities. Streamlines are shown in the top panels. The distance scale is in AU.

and $n_\infty(H^+) = 4 \times 10^{-3}$ cm^{-3}, suggest a pressure of $P/k \approx 4000$ cm^{-3} K, taking into account the pressure contribution from electrons in the fully ionized plasma. This is in better agreement with the low pressures suggested by the warm clouds within the LB than with the *ROSAT* estimates, but other models experiment with much higher densities and temperatures, in better agreement with the high *ROSAT* measurements (see Table 1 and § 4).

We also need to know the flow vector for the ISM around α Tau. The LIC flow vector is known very well (Lallement et al. 1995), so we can use that as one estimate. When combined with α Tau's known proper motion and radial velocity, the LIC vector suggests that α Tau sees an ISM flow speed of $V_\infty = 34$ km s^{-1}, with our line of sight to the star at an angle of $\theta = 149°$ with respect to the upwind direction of the ISM flow. However, the LIC vector may not apply to the hot ISM within the LB. Another approach is to assume that the hot ISM is at rest with respect to the local standard of rest (LSR). The LB was presumably created by a series of supernova explosions (Maíz-Apellániz 2001; Berghöfer & Breitschwerdt 2002). Since the hot stars that produce supernovae generally have low proper motions relative to the LSR, it is possible that the hot ISM within the Local Bubble is basically at rest in the LSR. If this is the case, then we estimate $V_\infty = 44$ km s^{-1} and $\theta = 170°$, taking into account the solar motion with respect to the LSR (Dehnen & Binney 1998). The LIC and LSR assumptions lead to similar values of V_∞ and θ, with both predicting that our line of sight to α Tau is very much through the downwind tail of the astrosphere. We experiment with both vectors in our astrospheric modeling (see Table 1).

4. MODELS OF THE α TAU ASTROSPHERE

4.1. *Hydrodynamic Modeling*

We model the α Tau astrosphere using two-dimensional, axisymmetric hydrodynamic codes developed to model the heliosphere and solar-like astrospheres. Most of our models are "two fluid" models like those described by Pauls et al. (1995). One fluid is used for the protons and another fluid for the neutral H. Treating the neutrals and plasma as separate fluids allows them to be out of thermal equilibrium with each other, which is the case in the heliosphere thanks to a collisional mean free path much larger than the size of the heliosphere. It is through charge exchange processes rather than collisions that neutrals take part in the heliospheric interaction. Figure 2 shows density distributions, temperature distributions, and flow patterns for the protons and H atoms in model 1.

The astrospheric structure of α Tau is in many respects similar to that of the heliosphere (see, e.g., Zank 1999). The stellar wind expands radially until it reaches a termination shock (TS), the roughly circular boundary seen about 1000 AU from the star in Figure 2. Prior to encountering the TS, the stellar wind is assumed to cool adiabatically while expanding outward, until it reaches 3 K (the cosmic background radiation temperature). At the TS,

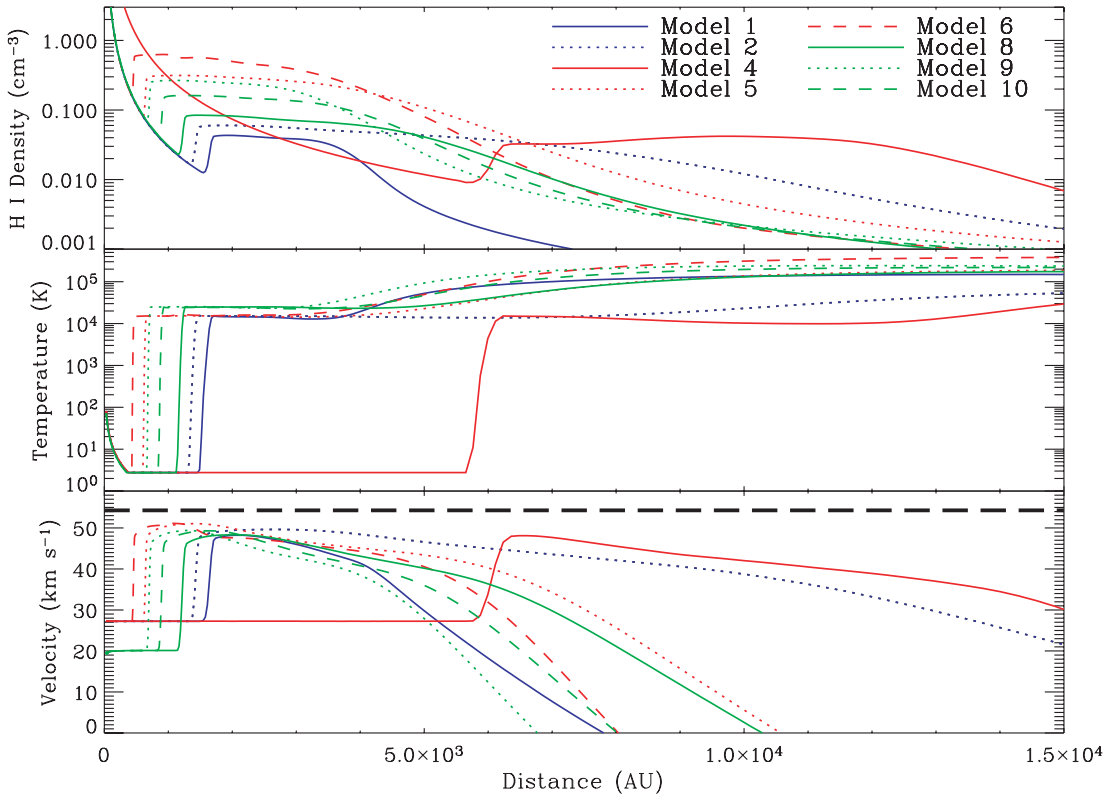

FIG. 3.—H I density (*top*), temperature (*middle*), and heliocentric velocity (*bottom*) vs. distance from the star along our line of sight to α Tau, for various two-fluid models of α Tau's astrosphere (see Table 1). The horizontal dashed line in the velocity panel is the rest frame of the star.

the stellar wind is heated, compressed, and decelerated. Beyond the TS there is a parabolic-shaped boundary separating the plasma flows of the stellar wind and ISM, the "astropause" (analogous to "heliopause"), which extends beyond the field of view in the downwind direction (to the left in Fig. 2). There is no bow shock beyond the astropause in the upwind direction (to the right) like there is for the heliosphere. Unlike the solar case, the ISM flow seen by α Tau is not supersonic, mostly due to the high ISM temperature, so no bow shock should exist for α Tau.

We compute astrospheric Mg II absorption from these models for our observed line of sight, which is defined by the θ-values in Table 1. Figure 3 shows traces of H I density, temperature, and velocity for this line of sight for most of the two-fluid models listed in Table 1. Model 7 leads to results very similar to model 6, so it is not shown in the figure.

In order to compute Mg II absorption profiles from the line-of-sight quantities in Figure 3, we have to assume that Mg II is the dominant ionization state of Mg, and we assume a solar Mg abundance from Grevesse & Sauval (1998) to estimate Mg II densities from the H I and H^+ densities. Since Mg II is an ionized species, we expect its temperature and velocity to follow that of the protons instead of the neutral H atoms. However, for the two-fluid models we find that proton temperatures and velocities match the H I temperatures and velocities in Figure 3 fairly well, so this distinction matters little.

Figure 4 shows the opacity in the Mg II *k* line predicted by the same eight models shown in Figure 3. Narrow opacity peaks at 19 or 27 km s^{-1} can be ignored, and have been truncated in the figure. This is absorption from the stellar wind inside the TS, where the actual observed wind absorption is saturated (see Fig. 1). When compared with the observed opacity, we find that the models do indeed have a peak in opacity at roughly the right velocity (~50 km s^{-1}) to match the data. This provides strong theoretical support for the astrospheric interpretation of the absorption.

The opacity is mostly from the "astrosheath," the post-TS region where the stellar wind material has been heated, compressed, and decelerated after encountering the TS. The TS is easily seen in Figure 3, at distances of 400–1600 AU from the star in most models, but at about 6000 AU for model 4. The astrospheric Mg II absorption is therefore coming from material thousands of

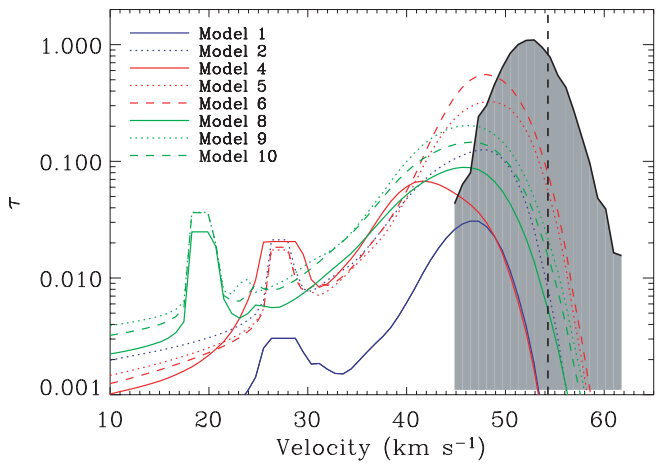

FIG. 4.—Opacity in the Mg II *k* line predicted by various models of the α Tau astrosphere (see Table 1), compared with the observed opacity (*shaded region*), plotted on a heliocentric velocity scale, as in Fig. 1. The vertical dashed line is the rest frame of α Tau. The narrow wind absorption at 19 or 27 km s^{-1}, which is not of interest here, has been truncated. The Mg II opacity at ~50 km s^{-1} predicted by the models is less than that observed and is not as close to the rest frame of the star.

AU from the star. The deceleration at the TS slows the outflow to velocities closer to the stellar rest frame, where the absorption is observed, and the jump in temperature to $T \sim 10^4$ K yields absorption with roughly the correct width to match the data.

With an orientation of $\theta = 149^\circ$–170°, our line of sight through the α Tau astrosphere is through its lengthy tail. We believe that the very downwind orientation of our line of sight through the α Tau astrosphere is the main reason that astrospheric absorption is detected for α Tau but not for other red giants. If we were observing an upwind or crosswind portion of the astrosphere (i.e., $\theta < 120^\circ$), the path through the heated post-TS material would be much shorter and the astrospheric absorption would be much weaker (see Fig. 2). It would be interesting to observe other red giants within the LB that have large, positive radial velocities, indicating downwind astrospheric orientations, in order to see if an astrospheric Mg II absorption signature could be found for other stars. Unfortunately, the apparent death of the STIS instrument on *HST* in 2004 August means that high-resolution UV spectroscopy is not currently possible, so such a project will have to await future instrumentation.

4.2. *Comparisons with the Data*

4.2.1. *Dependence on Stellar Wind Parameters*

Although the models predict an absorption peak in roughly the right location, the models are not able to match the data precisely. The predicted absorption is too weak and not close enough to the stellar rest frame (see Fig. 4). (The substantial underestimation of absorption is the reason why it is more practical to compare opacity profiles, as in Fig. 4, rather than absorption profiles.) Since the absorption is from decelerated post-TS stellar wind material, one might think that increasing the density of the stellar wind could significantly increase the predicted absorption and better match the data, but this is not the case.

Comparing models 1 and 4 in Figure 4 shows that a large factor of 10 increase in mass-loss rate yields only a modest increase in absorption. Furthermore, the resulting absorption profile is even more blueshifted from the observed profile than is the case for the other models. Increasing the stellar wind strength moves the TS farther from the star, such that the post-TS wind density remains essentially the same (see Fig. 3). Thus, the stronger wind of model 4 does not produce significantly more absorption despite an increase in wind density that is probably too large to be consistent with the wind absorption anyway (see § 2).

We find that lowering the ionization fraction of the wind also has little effect, since (as mentioned in § 4.1) model 7 produces essentially the same amount of absorption as model 6 despite a factor of 10 lower proton density (see Table 1). This is not surprising, since the wind is dominated by neutral H rather than protons. The stellar wind temperature has no effect on the properties of the post-TS material, since the thermal energy is small compared to the kinetic energy. In any case, by the time the wind reaches the TS, its temperature has decreased to the 3 K floor set by the background radiation (see § 4.1), meaning that the post-TS conditions are insensitive to the details of the thermal wind energy balance and the initial temperature. Models 8–10 demonstrate that increasing the stellar wind velocity (V_w) increases the post-TS temperature (see Fig. 3), but this by itself does not improve agreement with the data (see Fig. 4). Comparing models 5 and 10, where all parameters are equal except for V_w, shows that the stronger wind of model 10 pushes the TS outward, resulting in lower post-TS densities and weaker absorption than in model 5, worsening agreement with the data. We conclude that uncertainties in the stellar wind parameters are not likely the source of the hydrodynamic models' inability to precisely match the observed astrospheric absorption.

The models' underestimation of absorption is undoubtedly related to their underestimation of the amount of deceleration at the TS. Most of the $V_w = 27$ km s^{-1} models suggest a heliocentric post-TS velocity of $\sim$48 km s^{-1}. This is 6.3 km s^{-1} from the stellar rest frame at $V_{\rm rad} = 54.3$ km s^{-1}. Given the stellar wind velocity of $V_w = 27$ km s^{-1} at the current epoch, the implied degree of deceleration is a factor of 4.3, essentially at the strong shock limit of 4 for plane-parallel hydrodynamic shocks. However, the Mg II data imply a post-TS heliocentric velocity of 51.8 km s^{-1} (Redfield & Linsky 2002), which is only 2.5 km s^{-1} from the stellar rest frame, suggesting a deceleration factor of 10.8. The observations therefore suggest a factor of $f_{\rm dec} = 2.5$ times more deceleration at the TS than the models predict. For the $V_w = 35$ km s^{-1} models, $f_{\rm dec} = 3.3$. If we were to force an increase in TS deceleration in the models, conservation of mass would then lead to a corresponding increase in post-TS density, which would then increase the Mg II opacity, significantly improving agreement with the data in that respect as well. In § 4.3, we explore the possibility that radiative cooling is responsible for the unexpectedly strong deceleration at the TS.

4.2.2. *Dependence on the ISM Flow Vector*

Comparing models 1 and 2 shows that changing the ISM flow vector from the LIC vector to the LSR vector significantly increases the absorption. This is mostly because the LSR vector implies an even more downwind line of sight ($\theta = 170^\circ$) than the LIC vector ($\theta = 149^\circ$), resulting in a longer path length through the astrosheath (see Fig. 3). However, the absorption predicted by model 2 still falls well short of the observations, and changing the line-of-sight orientation does not improve the velocity discrepancy between the model absorption and the data.

Model 3 is a model computed with the same input parameters as model 2 but using a different approach to modeling the neutrals. The purpose of this model is to ensure that our lack of success in fitting the data is not due to an overly simplistic treatment of the neutrals in the two-fluid code. Charge exchange processes not only lead to neutral H velocity distributions different from those of the protons, but they can also lead to very non-Maxwellian distributions for the neutral H (Alexashov & Izmodenov 2005). Thus, a two-fluid treatment may not be sufficient. Ideally, the neutrals should be modeled with a fully kinetic code. Model 3 is a model that uses a fully kinetic Monte Carlo treatment of the neutrals, using a code developed for modeling the heliosphere described by Heerikhuisen et al. (2005, 2006).

Figure 5 compares the Mg II k line opacity predicted by the kinetic model 3 with the two-fluid model 2. When the Mg II ions are assumed to have velocity distributions like those of the protons, the predicted Mg II opacity of model 3 agrees reasonably well with that of model 2. Unlike in the two-fluid model, the neutral H and proton velocity distributions are quite different in the kinetic model, so Figure 5 also shows what the opacity profile looks like if the neutral H velocity distribution is used for Mg II. This greatly broadens and weakens the predicted absorption, worsening agreement with the observed absorption. The use of the kinetic code clearly does not improve agreement with the data, so we conclude that the two-fluid code's simple treatment of the neutrals is not to blame for our inability to precisely fit the data.

4.2.3. *Dependence on ISM Pressure*

Even though the material producing the absorption is fundamentally of a stellar wind origin rather than from the ISM, we find that the amount of absorption is more sensitive to changes in the

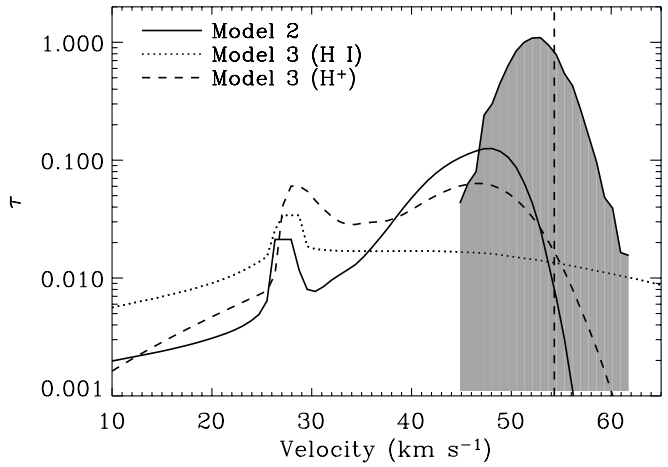

FIG. 5.—Opacity in the Mg II *k* line predicted by the two-fluid model 2 and the kinetic model 3, with identical input parameters (see Table 1). The dashed line assumes that the Mg II ions follow the velocity distribution of the protons in model 3, while the dotted line assumes that the Mg II ions follow the neutral H velocity distribution. The vertical dashed line is the rest frame of the star, and the shaded region is the observed Mg II opacity, as in Fig. 4.

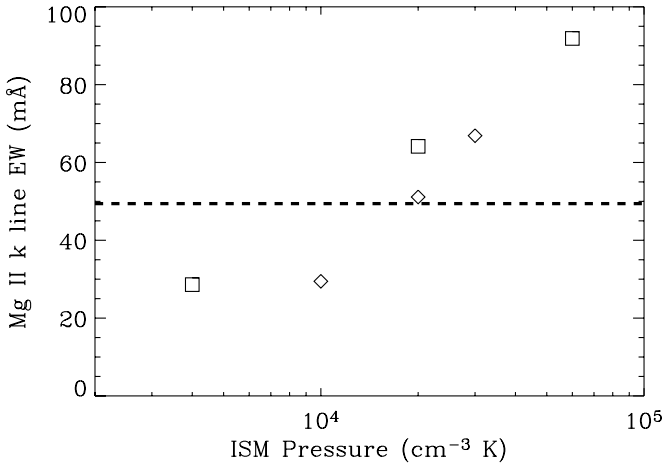

FIG. 6.—Mg II *k* line equivalent width (EW) predicted by three models with $V_w = 27$ km s^{-1} (models 2, 5, and 6; *squares*) and three models with $V_w = 35$ km s^{-1} (models 8, 9, and 10; *diamonds*), as a function of the ISM thermal pressure assumed in the models. The model predictions assume a solar Mg abundance, and we have increased the actual EWs predicted by the models by the $f_{\rm dec}$ mentioned near the end of § 4.2.1 to crudely correct for their underestimation of deceleration at the TS. The dashed line is the observed EW, suggesting an ISM pressure of 10,000–20,000 cm^{-3} K.

ISM pressure than to changes in stellar wind parameters. Comparing models 2 and 5 in Figure 4 shows that increasing the ISM density by a factor of 5 significantly increases the absorption. Comparing models 5 and 6 shows that a factor of 3 increase in ISM temperature yields a further increase in astrospheric absorption. The reason for the sensitivity of the absorption to ISM pressure is seen in Figure 3, which shows that higher ISM pressures (for models 5 and 6) push the TS closer to the star. Since stellar wind densities are then significantly higher when the wind encounters the TS, post-TS densities are also higher, resulting in stronger absorption. Unlike the heliosphere, which is confined solely by the ram pressure of the ISM flow, the α Tau astrosphere is confined by the hot ISM's thermal pressure, explaining why an ISM temperature increase is able to compress the astrosphere to a similar degree as a density increase.

Our results show that the astrospheric Mg II absorption is potentially valuable as an in situ diagnostic of the pressure of the hot ISM. Considering the difficulties in precisely measuring the LB pressure by other means, as described in § 3, additional LB pressure constraints would be valuable. Figure 6 plots the Mg II *k* line equivalent widths (EWs) predicted by three $V_w = 27$ km s^{-1} models (models 2, 5, and 6) and three $V_w = 35$ km s^{-1} models (models 8, 9, and 10) as a function of ISM pressure. We have increased the actual EWs predicted by these models by the $f_{\rm dec}$ factors mentioned near the end of § 4.2.1 to crudely correct for the underestimation of TS deceleration.

The actual Mg II *k* line EW measured from the data is 0.049 mÅ, which would suggest an ISM pressure of $P/k \sim$ 10,000–20,000 cm^{-3} K when compared with the model predictions in Figure 6. This is more consistent with the higher estimates mentioned in § 3. Unfortunately, there are substantial systematic uncertainties in this measurement. One is the ISM flow vector. If we changed from the LSR vector to the LIC vector, the model EWs in Figure 6 would decrease by about a factor of 7 based on comparing the results of models 1 and 2. This would yield EWs well below the observed value and suggest an ISM pressure of $P/k \gg 10^5$ cm^{-3} K. Clearly, any ISM pressure measurement from the astrospheric absorption is quite sensitive to the orientation of our line of sight through the α Tau astrosphere, which depends on the assumed ISM flow vector. The unreasonably high pressures suggested by the LIC vector imply that the LSR may be a more appropriate assumption for the hot ISM within the LB.

Another uncertainty is the Mg abundance in the stellar wind, which is assumed to be solar in the models. If we increased the Mg abundance by a factor of 2 the model EWs in Figure 6 would increase by a factor of 2 and the observed Mg II EW would then suggest $P/k < 10,000$ cm^{-3} K, more in line with the lower LB pressure estimates from measurements of warm cloud pressures (see § 3). There is some evidence that Mg may in fact be overabundant in α Tau's wind relative to solar abundances, based on the nondetection of astrospheric absorption in the O I λ1302 and C II λ1335 lines, which are discussed in § 5.

4.3. *Radiative Shock Modeling*

4.3.1. *Theoretical Foundation*

The location of the astrospheric absorption feature very close to the stellar rest frame appears to require that the compression ratio of the TS be significantly higher than the strong shock limit of 4 (see § 4.2.1). The only obvious way for a shock to do this is if it is a radiative shock, in which radiative cooling slows and compresses the flow beyond that allowed by a purely hydrodynamic shock (e.g., Raymond 1979). Converting our analytic, axisymmetric, two-fluid hydrodynamics code to a radiative hydrodynamics code would be onerous, so we instead rely on a simpler one-dimensional, single-fluid model to assess the possibility of a radiative TS. We are guided by Shu (1992) in the construction of this model.

A radiative shock can be divided into two parts, a standard hydrodynamic shock followed by radiative relaxation. The hydrodynamic shock is described by the Rankine-Hugoniot jump conditions, whose solutions are

$$\frac{\rho_2}{\rho_1} = \frac{V_1}{V_2} = \frac{(\gamma+1)M^2}{(\gamma+1)+(\gamma-1)(M^2-1)}, \quad (1)$$

$$\frac{T_2}{T_1} = \frac{[(\gamma+1)+2\gamma(M^2-1)][(\gamma+1)+(\gamma-1)(M^2-1)]}{(\gamma+1)^2M^2}, \quad (2)$$

where the subscripts 1 and 2 refer to pre- and postshock densities (ρ), velocities (V), and temperatures (T), respectively. We assume $\gamma = 5/3$ for a perfect gas. The Mach number, M, can be expressed as

$$M^2 = \frac{\mu m_p V_1}{\gamma k T_1}, \tag{3}$$

where m_p is the mass of the proton, k is the Boltzmann constant, and μ is a molecular weight factor that allows us to try to account for minority constituents of the gas, particularly electrons and He atoms. Assuming all electrons originate from H ionization,

$$\mu = \frac{1 + 4X_{\rm He}}{1 + X_{\rm He} + x_e}, \tag{4}$$

where $X_{\rm He} = 0.1$ is the fractional abundance of He, and x_e is the hydrogen ionization fraction.

In the radiative relaxation phase following the hydrodynamic shock, conservation of mass and momentum require that

$$\rho V = \text{constant}, \tag{5}$$

$$\rho V^2 + \frac{\rho k T}{\mu m_p} = \text{constant}. \tag{6}$$

These equations must be solved along with

$$\left(\frac{5}{2}\frac{\rho k T}{\mu m_p} - \frac{3}{2}\rho V^2\right)\frac{dV}{dx} = -\Lambda(T), \tag{7}$$

which expresses conservation of energy. In the temperature regime of interest here, the radiative cooling rate, $\Lambda(T)$, is entirely dominated by cooling from the Lyman lines of hydrogen. The total cooling rate is the sum of rates for each line, which individually have the form

$$\Lambda_i(T) = n_e n_{\rm H^0} E_i C_i(T) = \frac{\rho^2 x_e(1 - x_e)}{m_p^2(1 + 4X_{\rm He})} E_i C_i(T), \tag{8}$$

where n_e and $n_{\rm H^0}$ are the electron and neutral hydrogen densities, and E_i is the energy of the Lyman transition in question. The collision rate, $C_i(T)$, can be expressed (in cgs units) as

$$C_i(T) = \frac{8.6 \times 10^{-6}\Omega_i(T)}{g_1 T^{0.5}} \exp\left(-\frac{E_i}{kT}\right), \tag{9}$$

where $g_1 = 2$ is the statistical weight of the lower level of the Lyman transitions. We consider the four strongest Lyman lines, Lyα through Lyδ, in our models. The collision strengths for these lines, $\Omega_i(T)$, are taken from Aggarwal et al. (1991).

Finally, we track the ionization fraction of hydrogen, x_e, in the radiative relaxation phase via the equation

$$\frac{dx_e}{dx} = \frac{x_e \rho}{m_p V(1 + 4X_{\rm He})}\left[(1 - x_e)G(T)\exp\left(-\frac{E_{\rm ion}}{kT}\right) - x_e \alpha(T)\right], \tag{10}$$

where $E_{\rm ion} = 2.2 \times 10^{-11}$ ergs is the ionization energy of H. We extract the collision ionization function, $G(T)$, from Scholz & Walters (1991) and the radiative recombination rate, $\alpha(T)$, from Seaton (1959). In practice, we find that x_e does not change enough in the post-TS region to significantly affect the radiative relaxation.

4.3.2. *Model Results*

In order to illustrate how radiative shock structures depend on stellar wind speed and ionization, Figure 7 shows several models with different values of V_w and x_e. For these models we assume a total hydrogen density (including protons) entering the TS of $n_{\rm H} = 0.09$ cm^{-3}. Figure 3 shows that this pre-TS density is roughly appropriate for models 5 and 9, keeping in mind that the figure shows only the H I density, not including the minority proton constituents. The initial hydrodynamic termination shock is at 0 AU in Figure 7, while radiative relaxation occurs afterward. The initial shock shows the expected compression ratio of 4, the strong shock limit. Radiative cooling then leads to decreases in the post-TS flow velocity and temperature and to an increase in the compression ratio. However, only the $V_w = 35$ km s^{-1} models seem to produce enough deceleration to match the $\sim$2.5 km s^{-1} post-TS velocity suggested by the observations. Radiative cooling via the H Lyman lines is extremely temperature-sensitive. It is very efficient if the neutral H can be heated to $\sim$30,000 K, but temperatures this high are achieved only if $V_w \gtrsim 35$ km s^{-1}. In equilibrium conditions, hydrogen would simply ionize at these temperatures, but at the low densities that exist here radiative cooling occurs well before H can ionize.

If radiative processes are indeed responsible for the >4 compression ratio of α Tau's TS, then at least at the TS it must be true that $V_w \gtrsim 35$ km s^{-1} in order to get sufficiently hot post-TS temperatures. How can this be reconciled with the lower value of $V_w \approx 27$ km s^{-1} suggested by α Tau's wind absorption (see § 2)? We discuss three possibilities. The first is simply that V_w is underestimated in the wind absorption analysis due to oversimplified assumptions. One such assumption is that of constant turbulence throughout the wind acceleration region. If the turbulence decreases with increasing distance from the star, as indicated by the sharp Ca II H and K wind absorption features sometimes observed for α Tau, then the actual terminal velocity of the wind could be higher. A $V_w = 35$ km s^{-1} wind speed corresponds to a heliocentric velocity of about 19 km s^{-1}. This is still within the wind absorption core seen in Figure 1 and is therefore potentially consistent with the data.

The second explanation is that α Tau's wind continues to accelerate gradually beyond 27 km s^{-1}. Damping of the remnant magnetic wave energy that initiated the flow could drive the ionized wind component to higher velocities. For $x_e > 0.02$ the ion-neutral collision frequency, which is dominated by H^+-H resonant charge exchange, is smaller than the dynamical timescale within 25 R_*, where the Mg II k line has an optical depth of the order of unity. Therefore, the ion flow inside this radius continues to drag the more massive neutral wind out of the gravitational potential. A direct consequence of this is the heating of the wind flow by ambipolar diffusion heating (Ruden et al. 1990; Shang et al. 2002), in addition to any continued heating from MHD wave damping. We have computed the wind thermal structure for α Tau using the H^+-H scattering results of Glassgold et al. (2005) and find that ambipolar diffusion heating is an important term in the thermal balance. While the wind temperature at 1000 AU is higher than the 3 K floor assumed in our hydrodynamic models (see § 4.1), it remains sufficiently small that the wind thermal energy is not important at the TS.

The third and final explanation for the higher V_w suggested by the radiative shock models relies on the vastly different timescales represented by the wind and astrospheric absorption. The observed wind absorption happens within a few stellar radii of

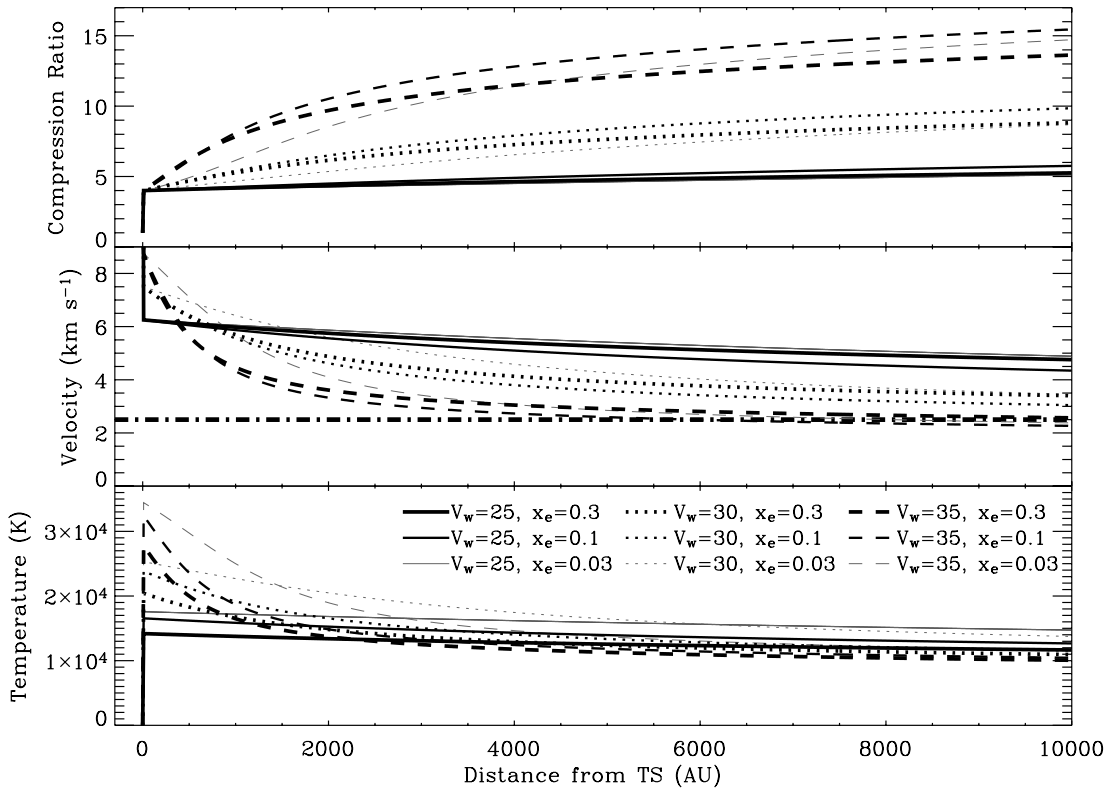

FIG. 7.—Radiative shock models of the compression ratio (*top*), flow velocity (in the stellar rest frame; *middle*), and temperature (*bottom*) as a function of distance from the termination shock. Models are shown assuming three different stellar wind speeds (V_w = 25, 30, and 35 km s^{-1}) and three different hydrogen ionization fractions (x_e = 0.03, 0.1, and 0.3). The horizontal dot-dashed line in the velocity panel is the observed location of the astrospheric absorption feature in Fig. 1. Only the shock models with V_w = 35 km s^{-1} show enough deceleration (i.e., high enough compression ratios) to reach the 2.5 km s^{-1} velocity suggested by this feature. [*See the electronic edition of the Journal for a color version of this figure*.]

the star and is therefore sensitive to mass loss on a timescale of months at most. In contrast, the astrospheric absorption is from an extended path length through wind material in the distant tail of α Tau's astrosphere, which will be sampling many thousands of years' worth of mass loss. Observations of optical Ca II lines show that α Tau's wind speed does vary, clearly exceeding 30 km s^{-1} at times (Reimers 1977; Kelch et al. 1978). Perhaps over the last many thousands of years $V_w \approx 35$ km s^{-1} has been more typical than the $V_w \lesssim 30$ km s^{-1} velocities more commonly seen in recent years.

The ionization fraction, x_e, affects the radiative cooling in two competing ways. High ionization corresponds with a lower μ, which leads to lower post-TS temperatures and therefore lower cooling rates (see Fig. 7). However, some ionization in the post-TS region is essential for radiative cooling because it is collisions with electrons that drive the Lyman line emission. In § 2 we mentioned that the ionization state of α Tau's wind is poorly constrained by observation. If radiative processes are indeed responsible for the >4 compression ratio of α Tau's TS, as we suspect, then our radiative shock models suggest that the wind must have $x_e \geq 0.03$ in order to provide sufficient radiative cooling in the post-TS region.

Based on these results, we have good reason to believe that radiative models of the α Tau TS significantly improve our ability to fit the data, at least if $V_w \geq 35$ km s^{-1} and $x_e \geq 0.03$. However, actually computing Mg II absorption from our one-dimensional radiative shock models for comparison with the data is not really possible, since these models do not consider the divergence of the actual three-dimensional wind. Another problem is that beyond the TS the flow is no longer radial, so our line of sight no longer follows a single streamline. We try to crudely correct for these problems by combining the radiative shock calculations with our axisymmetric hydrodynamic models, which properly represent the actual flow geometry.

Figure 8 shows how this is done for models 8 and 9. The thin lines show the shock structures of the original models. We compute radiative shock models appropriate for these two models, assuming the same $V_w = 35$ km s^{-1} and $x_e = 0.1$ values used in models 8 and 9 (see Table 1). We assume a pre-TS hydrogen density of $n_{\rm H} = 0.03$ cm^{-3} for model 8 and $n_{\rm H} = 0.09$ cm^{-3} for model 9. These are the pre-TS densities predicted by the astrospheric models (see Fig. 3), considering both the majority H I and minority H^+ constituents. The resulting post-TS velocity and temperature profiles of the radiative shock models completely replace those of the hydrodynamic code in the modified models in Figure 8. For the density profiles, we divide the compression ratio profiles suggested by the radiative shock models by 4 (the strong shock limit applicable to the purely hydrodynamic models) and then multiply that by the hydrodynamic model density profiles to get the modified density profiles shown in Figure 8.

Figure 9 shows the Mg II k line opacity profiles of the original models 8 and 9 and those of the models modified by the radiative shock calculations. The modified models clearly fit the data much better. The centroids of the opacity profiles are much closer to the observed one, and the modified models significantly increase the opacity, which also improves the fit to the data. However, only the modified model 9 truly comes close to precisely fitting the data. This model is still too blueshifted to a small degree, but the discrepancy may be consistent with the $\sim$1 km s^{-1} systematic

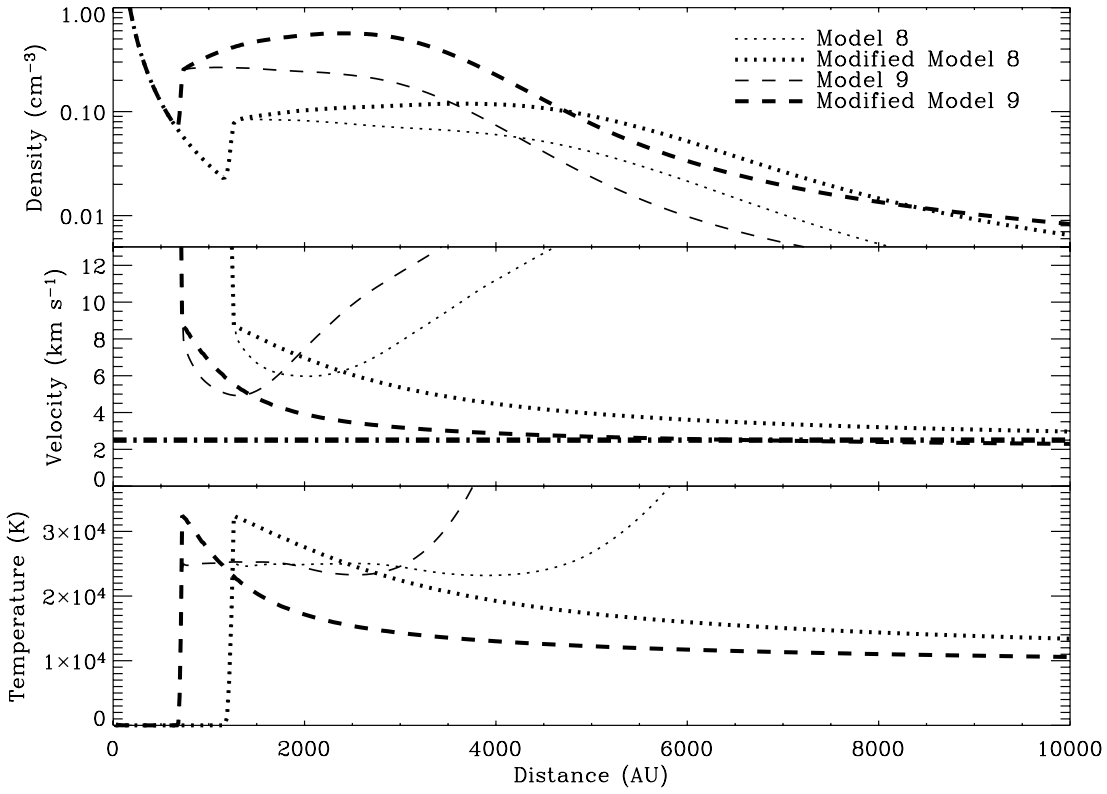

FIG. 8.—Traces of density (*top*), velocity (in the stellar rest frame; *middle*), and temperature (*bottom*) as a function of distance from the star, based on hydrodynamic models 8 and 9 (see Table 1), as well as for modified models based on radiative shock calculations (as in Fig. 7).

uncertainty in the wavelength calibration of the spectrum. The amount of absorption is still slightly underestimated, but uncertainties in the Mg abundance could easily account for that, particularly since there is some evidence that Mg may be overabundant relative to C and O (see § 5).

Based on Figure 9, model 9 would appear to be our best fit to the data. However, this model assumes an ISM thermal pressure of $P/k = 30{,}000$ cm^{-3} K, which seems implausibly high based on other measurements within the LB (see § 3). Model 8 assumes a more reasonable $P/k = 10{,}000$ cm^{-3} K, but this model is clearly less successful at producing sufficient astrospheric absorption. This lower ISM pressure places the TS farther from the star, resulting in lower post-TS densities that not only lead directly to less absorption but also make it difficult for radiative cooling to sufficiently decelerate the flow (see Fig. 8). Perhaps the greater success of the high-pressure models indicates significant pressure contributions from nonthermal sources, possibly magnetic pressure or cosmic-ray pressure. It might also be an indication that our models of the α Tau TS are still missing physics of an indeterminate nature.

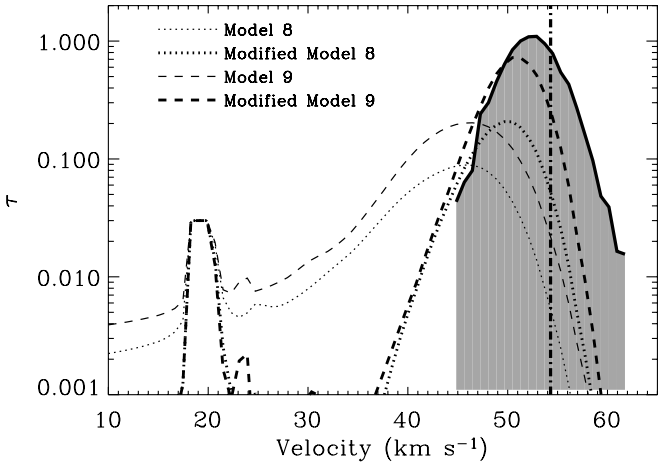

FIG. 9.—Opacity in the Mg II k line predicted by the models in Fig. 8, compared to the observed opacity (*shaded region*). As in Fig. 4, the wind absorption at 19 km s^{-1} is truncated. The vertical dot-dashed line is the rest frame of the star. The modifications made to the models based on the radiative shock calculations clearly improve agreement with the data, although only the modified model 9 truly comes close to matching the observed opacity.

5. THE O I AND C II NONDETECTIONS

Figure 10 shows the O I λ1302 and C II λ1335 lines observed by *HST* STIS. The broad wind absorption features appear very similar to those seen for the Mg II lines in Figure 1, but unlike Mg II there is no narrow astrospheric absorption feature at 51.8 km s^{-1}. The figures also shows various estimates of the astrospheric absorption that we would expect to see in the O I and C II lines based on the Mg II detection, assuming oscillator absorption strengths from Morton (2003).

There is evidence that α Tau has undergone first dredge-up, reducing the photospheric carbon abundance from its main-sequence value. Smith & Lambert (1985) find absolute logarithmic C and O abundances of 8.38 and 8.77 (using the convention of abundances scaled relative to $\log A_{\rm H} \equiv 12$). These abundances are 28% and 13% below the Grevesse & Sauval (1998) solar values, respectively. Redfield & Linsky (2002) measured a column density (per square centimeter) of $\log N_{\rm Mg} = 12.20$ from the Mg II absorption. Scaling from this measurement, the dot-dashed lines in Figure 10 show the predicted absorption for C II and O I assuming a solar abundance for Mg and the Smith & Lambert

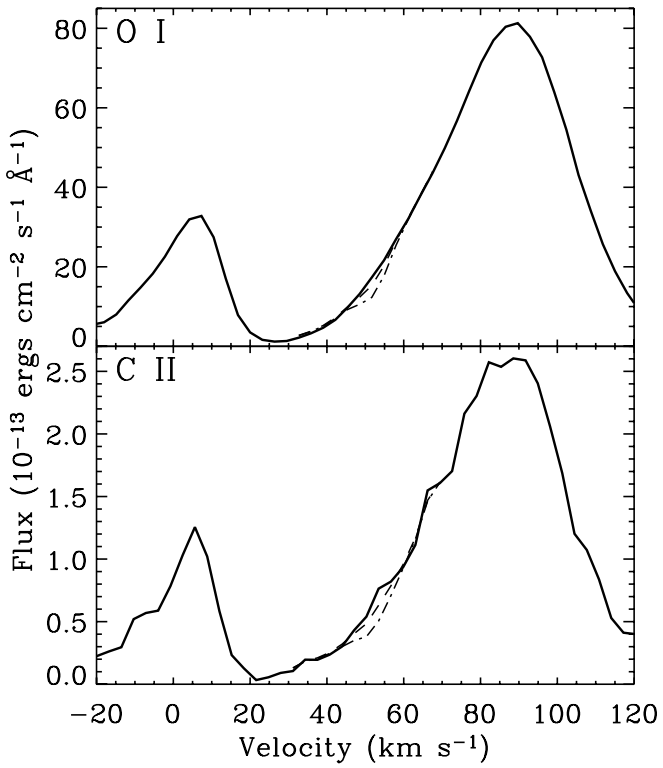

FIG. 10.—O I λ1302 and C II λ1335 lines of α Tau (*solid lines*). The lines show essentially the same broad wind absorption features as those seen in Mg II *h* and *k* (see Fig. 1), but they do not show the astrospheric absorption feature at 51.8 km s^{-1}. The dot-dashed lines show the expected absorption based on the strength of the astrospheric Mg II absorption, assuming C and O abundances from Smith & Lambert (1985) and a solar Mg abundance. The dashed lines show the expected absorption if the O and C abundances are reduced by a factor of 2.5 relative to Mg.

(1985) abundances for C and O. We have broadened the absorption features using a line-spread function appropriate for STIS E140M data. Since STIS E140M does not have the spectral resolution of the GHRS Ech-B grating, the predicted O I and C II absorption features appear broader than the observed Mg II absorption in Figure 1. The amount of absorption predicted for O I and C II amount to 11 and 3.5 σ detections, respectively. Thus, these predictions imply that we should be detecting astrospheric O I and C II absorption.

These estimates assume that O I and C II are the dominant ionization states of these elements in α Tau's wind, but these should be good assumptions. Charge exchange will tightly couple the ionization states of O and H, due to nearly identical ionization potentials. All evidence points to a predominantly neutral stellar wind (see § 2), so O should be mostly O I. As mentioned in § 2, there is no C I λ1656 wind absorption, and all evidence would suggest that the wind is too cool for C III, so C II is surely the dominant ionization state of C.

Unlike Mg II, O I is a neutral species. The kinetic model 3 predicts that astrospheric absorption from neutral species could be much broader than for ionized species (see Fig. 5). Significant broadening of the weak astrospheric absorption could make it undetectable for O I. However, this would not explain the C II nondetection.

The simplest way to resolve the problem with O I and C II is to propose that relative abundances within α Tau's wind are such that Mg is more abundant relative to C and O than the assumed abundances would suggest. This could be due to an intrinsically higher stellar Mg photospheric abundance, or it could be due to a fractionation effect such as the "first ionization potential" (FIP) effect observed for the Sun, in which the abundances of elements with low FIP (such as Fe, Si, and Mg) are enhanced in the solar wind and corona (Feldman & Laming 2000; von Steiger et al. 2000). Abundances reported by Luck & Challener (1995) suggest a photospheric Mg abundance somewhat above solar, although uncertainties are high. The dashed lines in Figure 10 show that a factor of 2.5 decrease in the O and C abundances, relative to Mg, would probably be just enough to explain the nondetections. This could correspond to either a factor of 2.5 abundance increase for Mg within α Tau's wind or a factor of 2.5 abundance decrease for C and O.

6. SUMMARY

We have constructed hydrodynamic models of α Tau's astrosphere in order to try to reproduce astrospheric Mg II absorption observed in *HST* spectra. Our findings are as follows.

1. The models demonstrate that stellar wind material that has been decelerated, heated, and compressed thousands of AU from the star at the TS can potentially explain the absorption, supporting the astrospheric interpretation.

2. However, the models are unable to reproduce the observed absorption precisely. The models underestimate the amount of absorption, and they predict too little deceleration at the TS. Changing from a simple two-fluid code to a more complex fully kinetic treatment of neutrals in the astrospheric interaction does not help. We propose that these problems can be solved by modeling the TS as a radiative shock, in which H Lyman line cooling leads to greater compression and deceleration downwind of the TS.

3. Simple one-dimensional radiative shock models are used to explore the nature of a radiative TS. Cooling sufficient to decelerate the wind to the observed post-TS speed is only obtained if α Tau's wind velocity is assumed to be at least $V_w = 35$ km s^{-1}. This is somewhat higher than our best estimates from α Tau wind absorption lines. Possible reasons for this discrepancy are variable wind turbulence, generally higher wind speeds in the distant past, and additional wind acceleration beyond the region of UV line formation. Sufficient deceleration is also obtained only if the H ionization fraction within α Tau's wind is $x_e > 0.03$. Finally, precisely fitting the data seems to require models that assume very high ISM pressures of $P/k \approx 30,000$ cm^{-3} K, seemingly inconsistent with lower pressures that have been estimated from X-ray background and LIC measurements. This could be an indication that our physical understanding of the α Tau TS is lacking in some way, such that our models are not yet able to precisely reproduce the structure of α Tau's TS, or perhaps it may indicate the presence of significant nonthermal pressure in the Local Bubble, possibly magnetic or cosmic-ray pressure, for example.

4. Our line of sight to α Tau is very much through the downwind portion of its astrosphere, but our lack of precise knowledge of the local ISM flow vector at α Tau means that there are significant uncertainties in its exact location. The amount of absorption predicted by the models is quite sensitive to the line-of-sight orientation. Absorption will be larger the more downwind the line of sight, due to a lengthier path through the tail of the astrosphere. The advantageous downwind direction of our line of sight is presumably why the astrospheric Mg II absorption is seen for α Tau, but not yet for any other red giant. At $\sim$1000 AU the TS presents an angular radius of $\sim 50''$. Direct imaging of the TS, if possible, would place limits on its apparent asymmetry in the sky, constraining the ISM flow vector.

5. Although the astrospheric absorption is fundamentally stellar wind rather than ISM material, the amount of absorption predicted by the models is not terribly sensitive to stellar wind parameters. The absorption is more sensitive to the ISM pressure. Thus, it is potentially a valuable ISM pressure diagnostic, and as mentioned above (see finding 3), the amount of observed absorption seems to be more consistent with rather high ISM pressures. However, uncertainties in the ISM flow vector and the Mg abundance within α Tau's wind preclude a precise pressure measurement.

6. The astrospheric absorption feature is only seen in the Mg II *h* and *k* lines. It is not seen in the O I λ1302 and C II λ1335 lines. This may imply that Mg is at least a factor of 2.5 more abundant in α Tau's wind relative to O and C than first dredge-up abundances would suggest.

We would like to thank J. Raymond for helpful discussions regarding radiative shocks and S. Drake for providing us with his radio measurements of α Tau. This work was supported by NASA grants NAG5-9041 and NNG05GD69G to the University of Colorado. G. M. H. was supported by NASA ADP grant NNG04GD33G and H.-R. M. by NASA ATP grant NAG5-13611, both issued through the Office of Space Science.

REFERENCES

Aggarwal, K. M., Berrington, K. A., Burke, P. G., Kingston, A. E., & Pathak, A. 1991, J. Phys. B, 24, 1385
Alexashov, D., & Izmodenov, V. 2005, A&A, 439, 1171
Ayres, T. R., Brown, A., & Harper, G. M. 2003, ApJ, 598, 610
Bellm, E. C., & Vaillancourt, J. E. 2005, ApJ, 622, 959
Berghöfer, T. W., & Breitschwerdt, D. 2002, A&A, 390, 299
Breitschwerdt, D. 2001, Ap&SS, 276, 163
Cravens, T. E. 2000, ApJ, 532, L153
Dehnen, W., & Binney, J. J. 1998, MNRAS, 298, 387
Drake, S. A., & Linsky, J. L. 1986, AJ, 91, 602
Feldman, U., & Laming, J. M. 2000, Phys. Scr., 61, 222
Florinski, V., Pogorelov, N. V., Zank, G. P., Wood, B. E., & Cox, D. P. 2004, ApJ, 604, 700
Glassgold, A. E., Krstic, P. S., & Schultz, D. R. 2005, ApJ, 621, 808
Gloeckler, G., Fisk, L. A., & Geiss, J. 1997, Nature, 386, 374
Grevesse, N., & Sauval, A. J. 1998, Space Sci. Rev., 85, 161
Harper, G. M. 2001, in ASP Conf. Ser. 223, Cool Stars, Stellar Systems, and the Sun, ed. R. J. Garcia Lopez, R. Rebolo, & M. R. Zapatero Osorio, (San Francisco: ASP), 368
Harper, G. M., Brown, A., Ayres, T. R., & Sim, S. A. 2004, in IAU Symp. 219, Stars as Suns: Activity, Evolution and Planets, ed. A. K. Dupree & A. O. Benz (San Francisco: ASP), 651
Harper, G. M., Wood, B. E., Linsky, J. L., Bennett, P. D., Ayres, T. R., & Brown, A. 1995, ApJ, 452, 407
Heerikhuisen, J., Florinski, V., & Zank, G. P. 2006, J. Geophys. Res. Space Phys., 111, A06110
Heerikhuisen, J., Florinski, V., Zank, G. P., & Müller, H.-R. 2005, in Solar Wind 11/*SOHO* 16: Connecting the Sun and Heliosphere, ed. B. Fleck & T. H. Zurbuchen (ESA SP-592; Noordwijk: ESA), 339
Hurwitz, M., Sasseen, T. P., & Sirk, M. M. 2005, ApJ, 623, 911
Izmodenov, V., Alexashov, D., & Myasnikov, A. 2005, A&A, 437, L35
Jenkins, E. B. 2002, ApJ, 580, 938
Kelch, W. L., Chang, S.-H., Furenlid, I., Linsky, J. L., Basri, G. S., Chiu, H.-Y., & Maran, S. P. 1978, ApJ, 220, 962
Lallement, R. 2004a, A&A, 418, 143
———. 2004b, A&A, 422, 391
Lallement, R., Ferlet, R., Lagrange, A. M., Lemoine, M., & Vidal-Madjar, A. 1995, A&A, 304, 461
Lallement, R., Quémerais, E., Bertaux, J. L., Ferron, S., Koutroumpa, D., & Pellinen, R. 2005, Science, 307, 1447
Lallement, R., Welsh, B. Y., Vergely, J. L., Crifo, F., & Sfeir, D. M. 2003, A&A, 411, 447
Luck, R. E., & Challener, S. L. 1995, AJ, 110, 2968
Maíz-Apellániz, J. 2001, ApJ, 560, L83
Morton, D. C. 2003, ApJS, 149, 205
Pauls, H. L., Zank, G. P., & Williams, L. L. 1995, J. Geophys. Res., 100, 21595
Perryman, M. A. C., et al. 1997, A&A, 323, L49
Raymond, J. C. 1979, ApJS, 39, 1
Redfield, S., & Linsky, J. L. 2000, ApJ, 534, 825
———. 2002, ApJS, 139, 439
———. 2004a, ApJ, 602, 776
———. 2004b, ApJ, 613, 1004
Reimers, D. 1977, A&A, 57, 395
Richichi, A., & Roccatagliata, V. 2005, A&A, 433, 305
Robinson, R. D., Blackwell, J., Feggans, K., Lindler, D., Norman, D., & Shore, S. N. 1992, A User's Guide to the GHRS Software, Ver. 2.0 (Greenbelt: GSFC)
Robinson, R. D., Carpenter, K. G., & Brown, A. 1998, ApJ, 503, 396
Ruden, S. P., Glassgold, A. E., & Shu, F. H. 1990, ApJ, 361, 546
Scholz, T. T., & Walters, H. R. J. 1991, ApJ, 380, 302
Seaton, M. J. 1959, MNRAS, 119, 81
Sfeir, D. M., Lallement, R., Crifo, F., & Welsh, B. Y. 1999, A&A, 346, 785
Shang, H., Glassgold, A. E., Shu, F. H., & Lizano, S. 2002, ApJ, 564, 853
Shu, F. H. 1992, The Physics of Astrophysics, Vol. II: Gas Dynamics (Mill Valley: University Science Books)
Smith, V. V., & Lambert, D. L. 1985, ApJ, 294, 326
Snowden, S. L., Egger, R., Finkbeiner, D. P., Freyberg, M. J., & Plucinsky, P. P. 1998, ApJ, 493, 715
Stone, E. C., Cummings, A. C., McDonald, F. B., Heikkila, B. C., Lal, N., & Webber, W. R. 2005, Science, 309, 2017
von Steiger, R., et al. 2000, J. Geophys. Res., 105, 27217
Wendker, H. J. 1995, A&AS, 109, 177
Wood, B. E., Linsky, J. L., Hébrard, G., Williger, G. M., Moos, H. W., & Blair, W. P. 2004, ApJ, 609, 838
Wood, B. E., Müller, H.-R., Zank, G. P., Linsky, J. L., & Redfield, S. 2005a, ApJ, 628, L143
Wood, B. E., Redfield, S., Linsky, J. L., Müller, H.-R., & Zank, G. P. 2005b, ApJS, 159, 118
Zank, G. P. 1999, Space Sci. Rev., 89, 413